Phase transformations and electrochemical characterizations of electrodeposited amorphous Fe–W coatings

Song Wang [a,b], Cheng Zeng [b], Yunhan Ling [b], Jianjun Wang [a], Guiying Xu [a,*]

[a] Laboratory of Special Ceramics and Powder Metallurgy, University of Science and Technology Beijing, Beijing 100083, China
[b] Laboratory of Advanced Materials, Tsinghua University, Beijing 100084, China

ABSTRACT

Iron–tungsten with satisfactory corrosion properties is a promising alloy to replace hard chromium. In this work, Fe–W amorphous coatings were prepared by electrodepositing from an aqueous solution and a subsequent heat treatment at 400 °C, 500 °C, 600 °C, 700 °C and 800 °C, respectively. Corrosion behavior of the coatings deposited on copper substrates was studied using potentiodynamic polarization and impedance spectroscopy techniques in $0.1 \, mol \cdot L^{-1}$ aqueous NaCl solution. As the annealing temperature raises the corrosion resistance of Fe–W coatings increases, and reaches the maximum at 500 °C and then shows a converse variation after 500 °C. This might relate to the surface reconstruction both on the morphology and the chemical oxidation.

© 2015 Elsevier B.V. All rights reserved.

1. Introduction

The interest in electrodeposition of iron–tungsten alloys has increased rapidly in recent years due to their hardness, corrosion resistance, and thermal resistance [1–3]. They can substitute for hard Cr coatings which are manufactured in environmentally hazardous processes based on hexavalent Cr.

It is commonly accepted that pure tungsten cannot be electrodeposited from aqueous solution because the electrodeposition of pure tungsten coating from tungstate solutions is hindered by the formation of an oxide layer on the cathode during electrodeposition. This oxide layer cannot be reduced to metallic tungsten directly because of the very low over-voltage for hydrogen evolution on tungsten [1,4]. But tungsten can be co-deposited with iron-group metals [5–8]. This phenomenon is called "induced co-deposition" by Brenner [9,10].

Various techniques are used for the synthesis of amorphous Fe–W alloy such as electroplating, mechanical alloying [11], electrochemistry [12], etc. Amid all the feasible techniques, electroplating provides the quickest and most efficient way of preparing the metallic thin films.

Y. Nishi and co-workers investigated the effects of pH and current density on the electroplating process for Fe–W coatings [2]. Y. Suwei et al. compared the corrosion resistance of Fe–W coating in NaCl solution and acid solution [13]. More studies on amorphous coatings have been reported in recent years, mainly focused on the corrosion properties of the amorphous coating at room temperature [14]. Nevertheless,

rare attention has been paid to the corrosion resistance of the Fe–W coatings after vacuum heat treatment. In addition, little is known about the influence of vacuum heat treatment on the phase and morphology and evolution of the electro-deposited Fe–W films. In this work, the corrosion behavior of the as-deposited and vacuum annealed Fe–W coatings was studied in 0.1 M NaCl solution by potentiodynamic polarization and electrochemical impedances spectroscopy (EIS) methods. The evolution of crystallographic structure, morphology and composition of the Fe–W coating aroused by vacuum annealing was also investigated.

2. Experiment

2.1. Electrodeposition

Fe–W amorphous alloys were electrodeposited in an aqueous bath containing $0.018–0.036 \, mol \cdot L^{-1}$ Na_2WO_4 and $0.212–0.243 \, mol \cdot L^{-1}$ $FeSO_4$ as the metal sources, $0.26 \, mol \cdot L^{-1}$ $(NH_4)_2C_4H_4O_6$ as the complexing agent based on the previous works [15]. The pH of the prepared bath was around 8.0 adjusted by adding sulphuric acid and the plating temperature was maintained at 60 °C. All of the solutions were prepared from analytical grade ($Na_2WO_4 \cdot 2H_2O$, $FeSO_4 \cdot 7H_2O$, $(NH_4)_2C_4H_4O_6$, H_2SO_4) components, and triple distilled water. Fe–W amorphous alloys were prepared using pulsed current with a rectangular waveform, having a 100 ms current on-time at a current density of $0.05 \, A \, cm^{-2}$, and 20 ms current off-time at a current density of $0.02 \, A \, cm^{-2}$. The specimens were electrodeposited on copper ($20 \times 10 \times 1 \, mm^3$), which was first electrochemically polished in

phosphoric acid and then ultrasonically cleaned in deionized water, acetone and alcohol, respectively. A two-electrode cell with an inert graphite as anode, while the above substrates as cathode was designed.

2.2. Heat treatment

The amorphous samples were subjected to heat treatment with a heating rate 10 °C min^{-1} at 400 °C, 500 °C, 600 °C, 700 °C and 800 °C for 60 min, under a controlled vacuum atmosphere(1.0×10^{-3} Pa), and then the samples were cooled to room temperature within the furnace.

2.3. Microstructure characterization and phase transformation analysis

The surface morphology and chemical composition of the Fe–W alloy coatings before and after annealing were analyzed using a field emission scanning electron microscopy (FESEM, JSM-7001F) equipped with an energy dispersive spectrometer X-ray (EDS). The phase compositions and grain sizes were identified by X-ray diffractometer (XRD, D/max 2500 with Cu Kα radiation) operating at 20 kV and 40 mA. A 0.02° step size X-ray spectra was collected in the 2θ range from 10° to 90°. X-ray photoelectron spectroscopy (XPS, ESCALAB 250Xi, Thermo Fisher SCIENTIFIC, US) was used with a monochromatic Al X-ray source of 15 kV, 45 W. The pressure during XPS analysis was less than 1×10–6 Pa and all spectra were referenced to C 1 s peak of adventitious

hydrocarbon at 284.60 eV [16]. The XPS spectra are curve-fitted with a combination of Gaussian and Lorentzian line shapes, using Shirley-type or Linear-type background substration.

2.4. Electrochemical corrosion studies

The electrochemical corrosion behavior was investigated by electrochemical impedance spectroscopy (EIS) and potentiodynamic polarization using a Zahmer IM6E computer-controlled potentiostat under open circuit conditions.

All electrochemical measurements were implemented in a three-electrode cell, in which the as-annealed samples acted as the working electrode, a platinum foil as the counter electrode, and a saturated calomel electrode (SCE) as the reference electrode. The front surface of the work electrode was sealed by epoxy by leaving area of 1 cm^2. All the electrochemical measurements were carried out in 0.1 mol·L^{-1} aqueous NaCl solution.

The open circuit potential (OCP) evolution of the specimens versus immersion time was recorded, with the testing duration being 60 min and the interval being 1 s. Afterwards, the electrochemical impedance spectroscopy (EIS) measurement was carried out using 10 mV peak-to-peak sinusoidal perturbation with a frequency ranging from 1 mHz to 10 MHz. The EIS data were analyzed and fitted to appropriate electrical
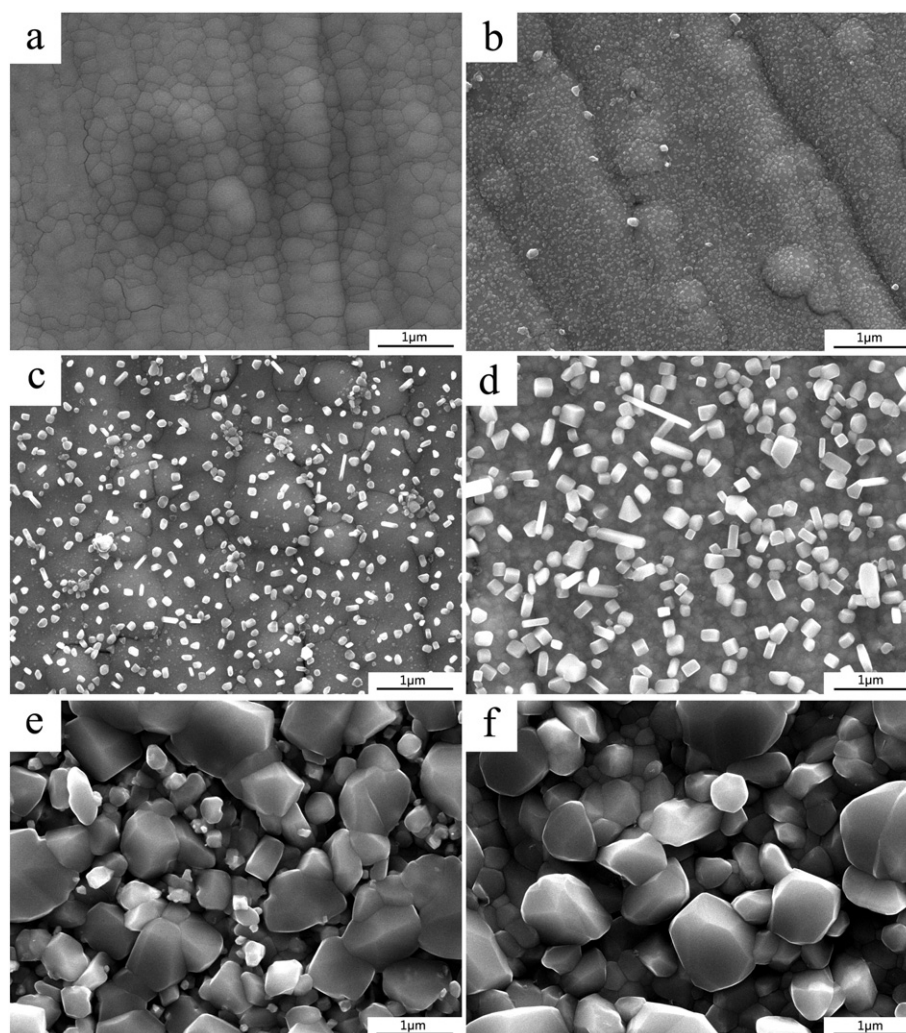
Fig. 1. FESEM images of as-deposited (a) and heat-treated Fe–W coating in vacuum at 400 °C (b), 500 °C (c), 600 °C (d), 700 °C (e), 800 °C (f).

equivalent circuit (EEC) using ZsimpWin software. The potentiodynamic polarization curves were recorded at a scan rate of 0.1667 mV·s^{-1}.

3. Results and discussion

3.1. Surface morphology

The morphologies of as-deposited and heat-treated Fe–W alloy coatings characterized by FESEM are displayed in Fig. 1. As-deposited Fe–W coating contains homogeneous and bright nodules on its surface and it is free from microcracks. Fig. 1b, c, d, e and f shows the SEM images of the coating on the interlayer after heat treatment at 400 °C, 500 °C, 600 °C, 700 °C and 800 °C, respectively. It reveals that after heat treatment, the amorphous Fe–W structure crystallized, probably due to the high free energy of the amorphous system [17,18], which was conducible to crystallization and densification of the amorphous phase. Also, it is clear in Fig. 1 that the grains grew to a larger size with the rising annealing temperature. The crystallization process in essence can be divided into two major stages, i.e. nucleation and growth. Initially, the crystallization is mainly restrained by the nucleation barrier, and the limited energy provided by the temperature lower than 400 °C cannot overcome it, causing the amorphous morphology shown in Fig. 1a and b. Under temperature of 500 °C and 600 °C, fractional amorphous phase starts to nucleate, forming the scattered crystal phase as shown in Fig. 1c and d. When the temperature is higher than 700 °C, the crystallization is entirely completed, leading to the formation of micron-size crystals.

3.2. Structures of the coatings

3.2.1. XRD results

XRD patterns for Fe–W alloys before and after heat treatment are shown in Fig. 2. A broad peak around 42° can be observed for as-deposited Fe–W alloy, which indicates the amorphous nature of the deposit. The amorphous alloy structure must arise either because the deposition process produces mutually incoherent particles which are too small for the crystalline configuration to be formed energetically or because the atoms do not bond together in the arrangement required for crystalline long-range order [19]. Heat treatment process plays a very important role in structure change. As annealing temperature increases, the percent of crystalline structure is augmented. As shown in Figs. 1 and 2, after heat treatment at temperature 400 °C, patches of nano-crystallites emerges from the amorphous matrix. Then heat treatment at 500 °C and 600 °C gives rise to a further crystallization of the amorphous phase forming the crystal phase of α-Fe and Fe$_2$W. However, residue of the amorphous phase, as indicated by the broader peaks still exists. At the annealing temperature equal to or higher than 600 °C, amorphous phase disappears and the deposits are completely crystallized. Although it is assumed that the as-prepared coatings merely comprise of iron and tungsten species, the presence of carbon in bulk is proved to be unavoidable in the electroplating process. It has been previously reported that the formation of carbide, Fe$_6$W$_6$C, confirms that some kinds of citrate species are incorporated into the coating [20]. Additionally, concentration of probable carbon in iron–tungsten alloy is dependent on the relative concentration of citrate in the electroplating bath [21].

3.2.2. XPS results

To obtain the chemical composition of the coating surface layer (<10 nm), both low resolution survey and high resolution spectra of the Fe-2p, W-4f and O-1 s band regions were used. High resolution XPS spectra containing the Fe-2p and W-4f bands are shown in Fig. 3. The bonding energies for Fe^0 [22], FeO [23], Fe$_2$O$_3$ [24] and Fe$_3$O$_4$ [25] are 702.81, 710.3, 710.4 and 710.2 eV, respectively, and the binding energies for W^0 [26] and WO$_3$ [27] are 31 or 32.5, and 35.2 eV.
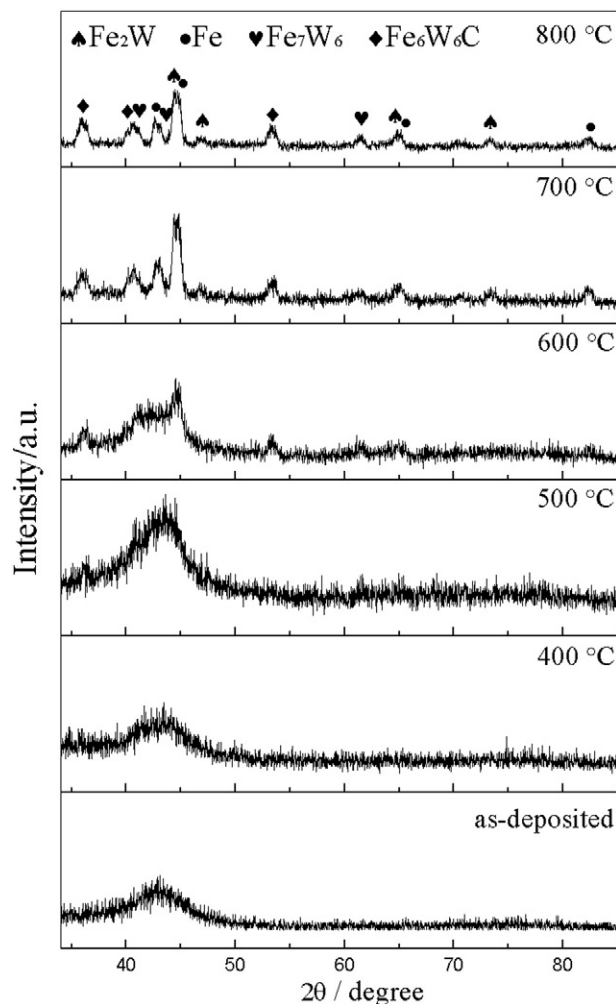

Fig. 2. XRD patterns for the investigated alloys.

The fitting results are presented in Tables 1 and 2. It is shown that for the as-deposited coating, iron mainly exists as iron oxide and tungsten exists as metallic tungsten. After 500 °C heat-treatment, the iron and tungsten on the surface appears to be completely oxidized. However, for sample annealing at 800 °C, the chemical state of fractional Fe-2p and W-4f components reverse back to the metallic state. It should be noted that an unknown component is identified with binding energy of Fe-2p centered at 714.8 eV.

3.3. Electrochemical corrosion studies

Corrosion behavior of the coating was evaluated using polarization and electrochemical impedance spectroscopy techniques. It is acknowledged that the corrosion resistance has a positive correlation with coating impedance, but a negative correlation with the corrosion current density (i_{corr}). In a typical polarization curve, the corrosion current density can be calculated by the Butler–Volmer equation. Fig. 4 shows potentiodynamic polarization curves recorded in 0.1 M NaCl solution for the as-deposited and heat-treated Fe–W coatings. The corrosion potential (E_{corr}) and corrosion current density (i_{corr}) obtained from the potentiodynamic polarization curves are listed in Table 3. Given that the anodic region of the Tafel curve does not show an accessible linear segment which can be used for the simulation process, an alternative method of cathodic extrapolation was employed to determine corrosion current density.
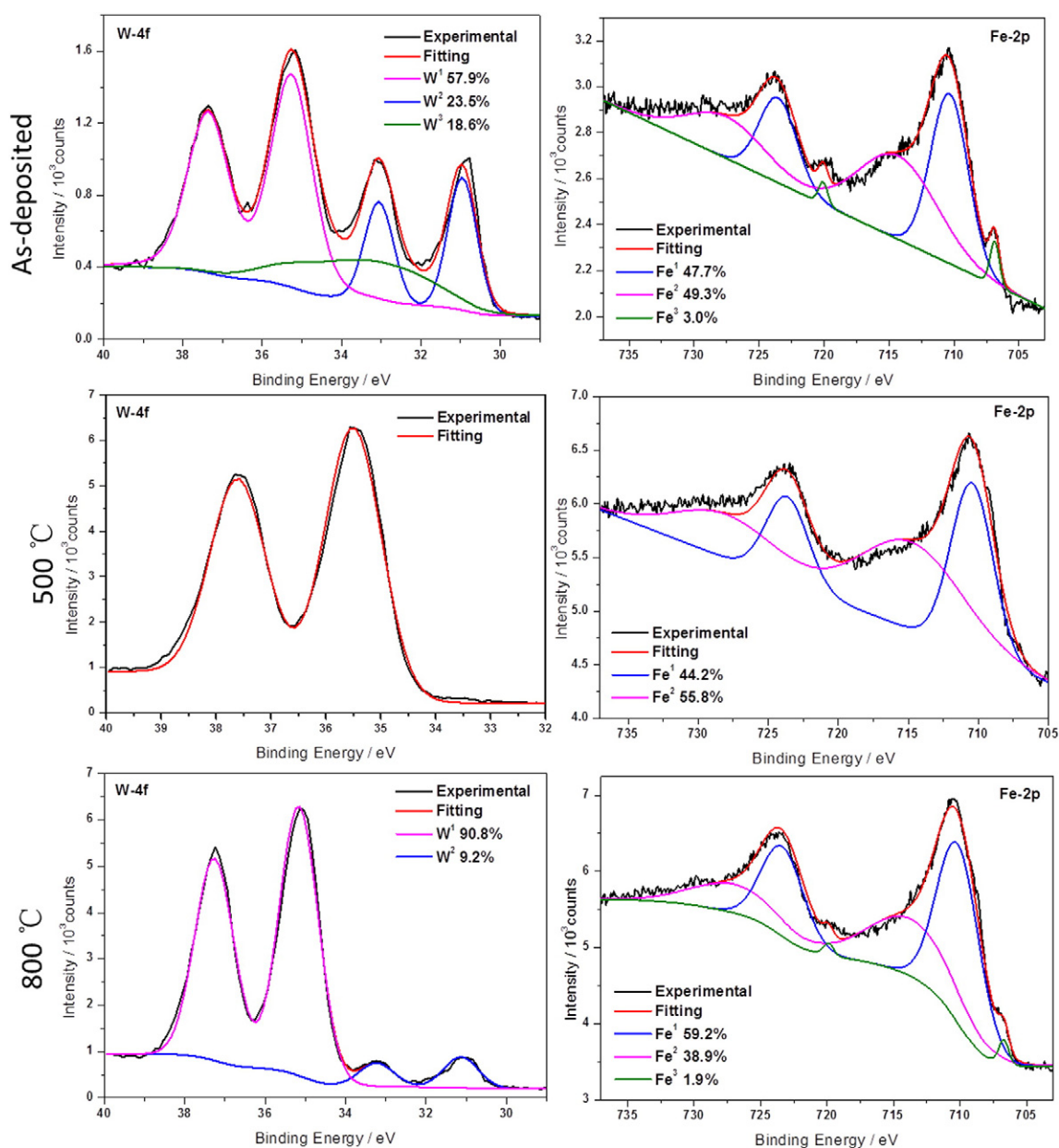
Fig. 3. High resolution XPS spectrum of the W-4f and Fe-2p band region.

As seen from Fig. 4 and Table 3, compared to that of the as-prepared specimen, i_{corr} of the coatings after heat treatment, except for the coating heated at 800 °C, decreased significantly. Therefore, the heat treatment can significantly increase the corrosion resistance of the investigated coatings. With the increasing annealing temperature, the i_{corr} decreases from 2.3143 μA·cm^{-2} for 400 °C to 1.5368 μA·cm^{-2} for 500 °C firstly, reaching a nadir at 500 °C, and then shows a one-direction increase from 1.5368 μA·cm^{-2} to 4.4838 μA·cm^{-2} with the temperature rising from 500 °C to 800 °C. Thus the Fe–W coating annealing at 500 °C has the largest corrosion resistance in terms of i_{corr}.

The effect of the annealing temperature was verified using the EIS technique. Nyquist diagrams and Bode diagrams for different annealing temperatures in 0.1 mol·L^{-1} aqueous NaCl solution are shown in Fig. 5a and b. Each point in the Nyquist plot represents impedance at a particular frequency. As seen from Fig. 5b, the bode plots for all the coating (except the sample annealed at 500 °C) show two time constants and thus it is concluded that there are two mechanism prevailed for the corrosion of the coatings. For the sample annealed at 500 °C, there are three time constants, which suggested that the amorphous phase coexisted with crystallite phase.

Table 1
Iron speciation as determined by XPS analysis.

Fe species	As-deposited %	500%	800%
Fe^0	3.0	0	1.9
Fe^{II}, Fe^{III}	47.3	44.2	59.2
Fe*	49.3	55.8	38.9

Table 2
Tungsten speciation as determined by XPS analysis.

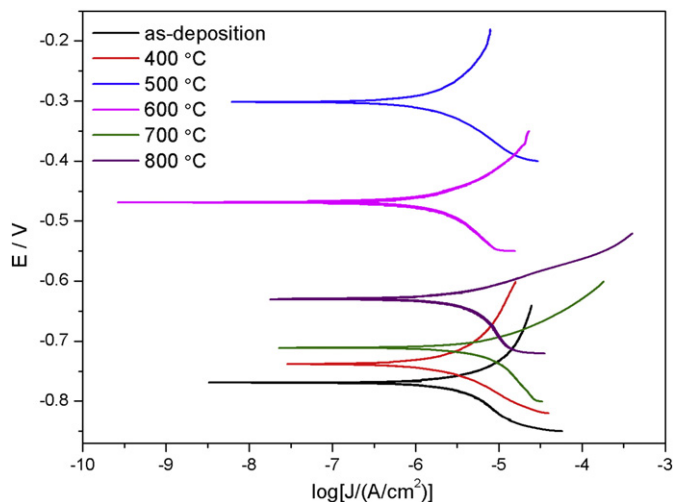| W species	As-deposited %	500%	800%
W^0	76.5	–	90.8
WO$_3$	23.5	100	9.2

Fig. 4. Potentiodynamic polarization curves for the investigated coatings obtained in 0.1 M NaCl.

Accordingly, the corresponding Randles equivalent circuits were applied in this work for curve fitting. The schematics of the circuits are shown in Fig. 6. The simulation parameters using ZsimpWin software are listed in Table 4. The equivalent circuit used to simulate the EIS results of as-deposited samples and samples annealing at 400 °C, is shown in Fig. 6a, comprising of parameters namely solution resistance (R_s), the double layer capacitance (C_{dl}), charge transfer resistance (R_{ct}), coating resistance (R_d), coating capacitance (C_d) and constant phase element (Q). R_s is the solution resistance between the reference and Cu electrode. It represents the ohmic resistance of the solution when ions move to the working electrode surface. C_{dl} represents the double layer capacitance of the electrolyte at the metal surface. Because of the inhomogeneity in the coating and metal surface, this capacitance is implemented as a Constant Phase Element (CPE). R_{ct} is the Faraday resistance (for charge transfer resistance) offered by the metal atom to get ionized when it contacted with the electrolyte. The equivalent circuit shown in Fig. 6b is proposed to fit EIS plots of the samples annealing from 500 to 800 °C. In this circuit, O refers to the semi-infinite diffusion resistance.

Generally, the higher the charge transfer resistance (R_{ct}), the greater the corrosion resistance system. The maximum value of R_{ct} (3175 $\Omega \cdot cm^2$) is obtained at 500 °C. After 500 °C, there is an obvious R_{ct} drop with the increase of temperature. On the basis of the comprehensive characterizations about phase structure, morphology and chemical states of the cations on the surface, t can be inferred that, compactness and grain sizes are the major factors to influence corrosion resistance of the annealed Fe–W alloys. Also, it should be noted that hydrogen-induced heterogeneous, cracks and probably other defects are also influential causes of the corrosion resistance loss. In comparison of the variation of i_{corr} and R_{ct} versus the temperature change, as shown in Tables 3 and 4, the i_{corr} results derived from the polarization curves are well consistent with the R_{ct} results drawn from the EIS data.

Based on all the results discussed above, it is assumed that the special variation of corrosion resistance is mainly ascribed to the compactness change and phase evolution of the Fe–W coatings. After annealing
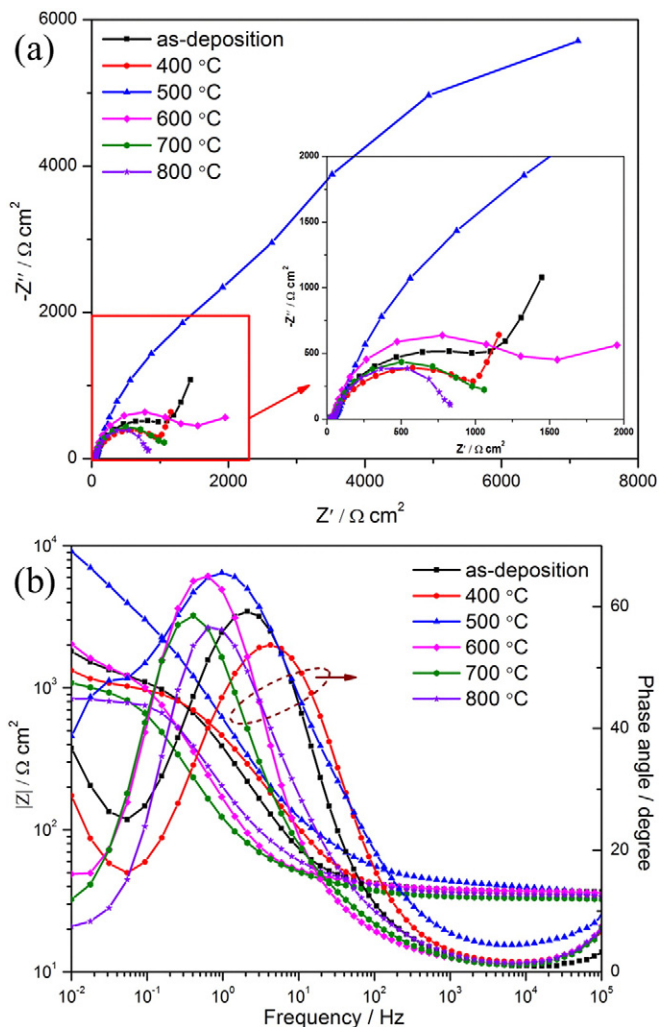

Fig. 5. Nyquist (a) and Bode plot (b) for as-deposition and the coatings annealed at different temperature.

at temperature lower than 500 °C, the amorphous coatings become more densified, and thus cause the gain of corrosion resistance, as shown in Fig. 1. Also, from the XPS results for samples annealing at 500 °C (Tables 1 and 2), a nanoscale thin oxide forms on the surface, which is probably the other reason for the maximum resistance at 500 °C. However, it should be mentioned that the heat treatment process is accompanied with nucleation and grain growth of crystals. It can be seen from XRD results (Fig. 2), the samples annealing at temperature lower than 500 °C are still predominately composed of amorphous phase. Thus, nucleation should be the dominant rate-controlled process rather than grain growth. Nevertheless, when the temperature is higher than 500 °C, nucleation barrier has been overcome and grains grow rapidly, leading to the formation of much less compact coatings, as shown in Fig. 1. Additionally, with increasing of the annealing temperature, the grain size further increases, and hence compactness of the coating decreases, causing a further loss of corrosion resistance.

Table 3

Corrosion parameters of the investigated coatings in 0.1 M NaCl solution derived from potentiodynamic polarization curves.

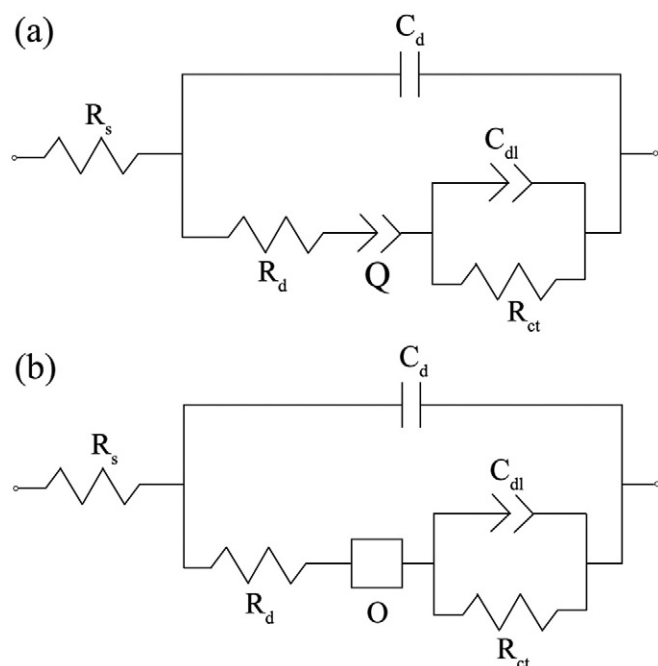| Coatings	As-deposited	400	500	600	700	800
E_{corr} (V)	−0.76975	−0.73807	−0.30141	−0.46902	−0.71157	−0.62955
i_{corr} ($\mu A/cm^2$)	2.7768	2.3143	1.5368	1.663	2.1431	4.4838

Fig. 6. Equivalent circuits for samples in 0.1 mol·L^{-1} NaCl solution.

Table 4
Simulated impedance parameters.

	R_s ($\Omega \cdot cm^2$)	C_d (F/cm^2)	R_d ($\Omega \cdot cm^2$)	R_{ct} ($\Omega \cdot cm^2$)/E[a]
As	9.007	5.155E−9	28.09	817/2.9
400	16.43	1.853E−8	19.17	985.5/1.3
500	15.05	1.542E−8	24	3175/6.8
600	16.12	1.713E−8	20.81	1418/1.3
700	14.75	1.867E−8	18.15	1046/1.3
800	15.09	1.761E−8	19.69	814.8/1.5

[a] E: error (%).

4. Conclusions

Homogenous Fe–W amorphous coatings were successfully fabricated by pulsed electrodepositing and a subsequent heat treatment at different temperature was implemented to investigate the effect of heating temperature on the corrosion behavior of these coatings.

From the electrochemical results, it is confirmed that the Fe–W coating annealing at 500 °C displayed the highest corrosion resistance, which could be a promising candidate for corrosion protection. In addition, based on the comprehensive characterization techniques, the underlying reason was discussed and proposed. It is concluded that the compactness change and the formation of a nanoscale film after annealing are accountable to this intriguing phenomenon.

References

[1] S.J. Mun, M. Kim, T.H. Yim, J.H. Lee, T. Kang, J. Electrochem. Soc. 157 (2010) D177.
[2] Y. Nishi, Y. Mogi, K. Oguri, J. Mater. Sci. Lett. 14 (1995) 1.
[3] M. Donten, H. Cesiulis, Z. Stojek, Electrochim. Acta 45 (2000) 3389.
[4] N. Tsyntsaru, J. Bobanova, X. Ye, H. Cesiulis, A. Dikusar, I. Prosycevas, J.P. Celis, Surf. Coat. Technol. 203 (2009) 3136.
[5] P.L. Neto, A.N. Correia, R.A.C. Santana, R.P. Colares, E.B. Barros, P.N.S. Casciano, G.L. Vaz, Electrochim. Acta 55 (2010) 2078.
[6] C.N. Tharamani, P. Beera, V. Jayaram, N.S. Begum, S.M. Mayanna, Appl. Surf. Sci. 253 (2006) 2031.
[7] N. Eliaz, T.M. Sridhar, E. Gileadi, Electrochim. Acta 50 (2005) 2893.
[8] M. Ahmadi, M.J. Guinel, J. Alloys Compd. 574 (2013) 196.
[9] M.C. Chou, C.F. Chu, S.T. Wu, Mater. Chem. Phys. 78 (2002) 59.
[10] A.L.M. Oliveira, J.D. Costa, M.B. Sousa, J.J.N. Alves, A.R.N. Campos, R.A.C. Santana, S. Prasad, J. Alloys Compd. 619 (2015) 697.
[11] T.D. Shen, K.Y. Wang, M.X. Quan, J.T. Wang, J. Appl. Phys. 71 (1992) 1967.
[12] T. Zak, O. Schnessweiss, D. Minic, J. Magn. Magn. Mater. 272-276 (2004) e1119.
[13] S.W. Yao, S.L. Zhao, L.B. Ren, H.T. Guo, M. Kowaka, Surf. Coat. Technol. 79 (1996) 205.
[14] U.P. Kumar, C.J. Kennady, Q.Y. Zhou, Surf. Coat. Technol. 283 (2015) 148.
[15] S. Wang, Y.H. Ling, P. Zhao, N.Z. Zang, J.J. Wang, S.B. Guo, J. Zhang, G.Y. Xu, Fusion Eng. Des. 88 (2013) 248.
[16] J.A. Rotole, P.M.A. Sherwood, Surf. Sci. Spectra 5 (1998) 46.
[17] V. Caron, Y. Hu, L. Tajber, A. Erxleben, O.I. Corrigan, P. Mcardle, A.M. Healy, Pharm. Sci. 14 (2013) 464.
[18] K. Greco, R. Bogner, Mol. Pharm. 7 (2010) 1406.
[19] F.J. He, J. Yang, T.X. Lei, C.Y. Gu, Appl. Surf. Sci. 253 (2007) 7591.
[20] R. Juskenas, I. Valsiunas, V. Pakstas, R. Giraitis, Electrochim. Acta 54 (2009) 2616.
[21] H. Alimadadi, M. Ahmadi, M. Aliofkhazraei, S.R. Younesi, Mater. Des. 30 (2009) 1356.
[22] C.E. Myers, H.F. Franzen, J.W. Anderegg, Inorg. Chem. 24 (1985) 1822.
[23] G.C. Allen, M.T. Curtis, A.J. Hooper, P.M. Tucker, J. Chem. Soc. Dalton Trans. (1974) 1525.
[24] V.I. Nefedov, Y.V. Salyn, G. Leonhardt, R. Scheibe, J. Electron Spectrosc. Relat. Phenom. 10 (1977) 121.
[25] B.J. Tan, K.J. Klabunde, P.M.A. Sherwood, Chem. Mater. 2 (1990) 186.
[26] W. Chen, J.T. Roberts, Surf. Sci. 324 (1995) 169.
[27] K.T. Ng, D.M. Hercules, J. Phys. Chem. 80 (1976) 2095.